NANO LETTERS

pubs.acs.org/NanoLett

Letter

Ultrathin, Stimuli-Responsive, Antimicrobial, Self-Cleaning, Reusable, and Biodegradable, Micro/Nanofibrous Electrospun Mat as an Efficient Face Mask Filter for Airborne Disease Prevention

Keya Ganguly, Aayushi Randhawa, Sayan Deb Dutta, Hyeonseo Park,
Mehran Mohammad Hossein Pour, Hojin Kim, Rumi Acharya, Tejal V. Patil, Beom-Soo Shin,*
Dae Hyun Kim,* and Ki-Taek Lim*

Cite This: *Nano Lett.* 2025, 25, 7641−7650

Read Online

ACCESS | Metrics & More | Article Recommendations | Supporting Information

ABSTRACT: A multifunctional, electrospun, ultrathin face mask is desirable for preventing disease spread while ensuring breathability. However, balancing ultrathin construction with antimicrobial efficacy is challenging. Here, we fabricated an ultrathin micro/nanofibrous electrospun matrix, consisting of three biodegradable polymer layers, for high antibacterial efficiency, breathability, and biodegradability. The outer layer, with an average thickness of 9.01 ± 3.1 μm, is composed of polycaprolactone (PCL), silver nitrate ($AgNO_3$), and β-cyclodextrin (β-CD). The middle layer, with a thickness of 4.61 ± 1.4 μm, comprises poly(vinyl alcohol) (PVA) and multiwalled carbon nanotubes (MWCNT) as a conductive layer. The inner layer, with a thickness of 5.12 ± 1.4 μm, contains PVA, carboxymethyl chitosan (CMC), and cellulose nanofibrils (CNFs) as a superabsorbent layer, supported by medical gauze. With a total thickness of ∼300 μm, the mask provides antibacterial efficacy, self-cleaning, reusability, mechanical stability, and biodegradability. This design advances filtering face masks, offering a solution to combat contagious diseases while minimizing environmental impact.

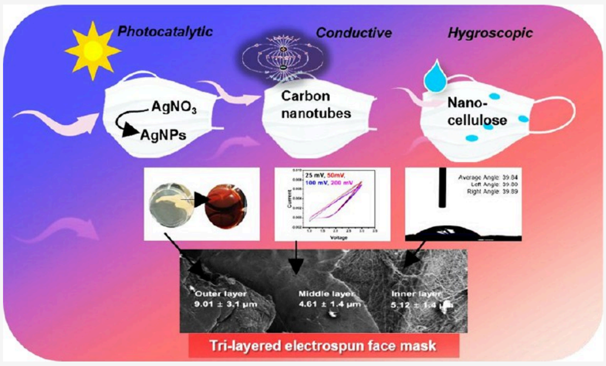

KEYWORDS: *ultrathin, face mask, electrospun matrix, antibacterial, breathable, biodegradable*

An unprecedented spread of airborne microbial diseases has caused severe acute respiratory syndromes. These include diseases caused by aerosolized bacteria,[1−3] such as *Streptococcus* spp., leading to outbreaks of respiratory illness.[4] These microbes are mutable and can develop drug-resistant variants.[5,6] Consequently, the development of effective face masks has been advancing. Face masks with plasmonic catalytic abilities have been fabricated to mediate reactive oxygen species (ROS)-induced antimicrobial efficiency.[7] Biomimetic tendril nanofibrous air masks are designed to filter particulate matter, including PM0.3 matter.[8] Other designs include web-like antimicrobial nanoporous fibers,[9] transparent face masks with copper nanowires for thermal sterilization,[10] and photoactive antiviral face masks made of shellac and copper nanoparticles for protection against bacteria and viruses.[11] However, the high cost of technologically advanced face masks forces most developing nations to rely on inefficient cloth masks.[12] Additional challenges associated with face masks include low reusability, a tendency to accumulate water during breathing, and issues with biodegradability.[13−15]

Herein, we developed a thin micro/nanofibrous electrospun mask (prototype) for exceptionally reliable antibacterial properties, stimuli-induced sterilizing ability, moisture-free air permeability, and biodegradability. The matrix is composed of three layers of biodegradable polymers. The outer layer is made of polycaprolactone (PCL), β-cyclodextrin (β-CD), and Silver Nitrate ($AgNO_3$) with an average thickness of 9.01 ± 3.1 μm, denoted as the PBA layer. The middle layer consists of poly(vinyl alcohol) (PVA) and multiwalled carbon nanotube (MWCNT) as a conductive layer measuring 4.61 ± 1.4 μm, denoted as the PM layer. The inner layer is composed of PVA, carboxymethyl chitosan (CMC), and cellulose nanofibrils (CNF) as a super absorbent layer with a thickness of 5.12 ± 1.4 μm on a gauge support, denoted as the PCC layer. The mask's overall thickness was limited to ∼ 300 μm, depending on the additional thickness of the support gauge. Each layer

Received: September 13, 2024
Revised: April 18, 2025
Accepted: April 25, 2025
Published: May 1, 2025

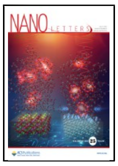

ACS Publications

https://doi.org/10.1021/acs.nanolett.4c04525

Scheme 1. Schematic Illustration of the Fabrication of a Trilayered Electroscope Antibacterial Face Mask[a]

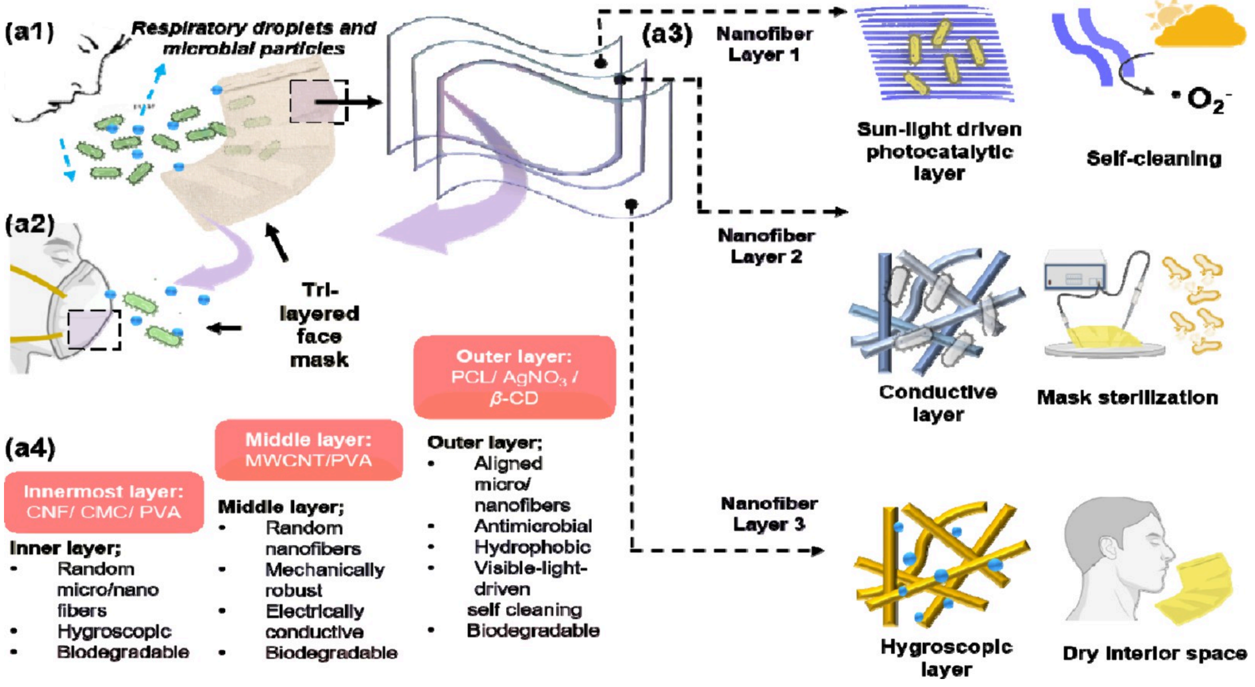

[a] (**a1**) Respiratory droplets and microbial particles discharged from infected person coming in contact with the trilayered nanofiber mask. (**a2**) Healthy person with fabricated nanofiber mask coming in contact with infectious bacterial particles. (**a3, a4**) The physiochemical characteristics and composition of the three layers of the face mask showing aligned fiber orientation and sunlight-induced photocatalytic property (outermost layer), randomly aligned conductive nanofiber layer (middle layer), and the cellulose nanofiber based ultra-hygroscopic layer (innermost layer).

offers unique advantages to fight infectious diseases while lowering environmental effects (Scheme 1).

First, we electrospun the three layers separately to evaluate their functionalities (Figure 1a). The surface morphologies of all the membranes were analyzed using scanning electron microscopy (SEM) as shown in Figure 1b. Since nanofiber orientation affects bacterial adherence, we chose certain orientations for each layer. The outer PBA layer comprised parallelly arranged PCL nanofibers incorporating β-CD and $AgNO_3$ with an average fiber diameter of 0.440 ± 0.05 μm (Figure 1b, upper panel). As shown in Supporting Information, Figure S1, the raw PCL fibers display a random arrangement of highly interconnected nanofibers, highlighting the role of the incorporated material in their alignment. The SEM-EDX spectra of the PBA layer revealed the uniform distribution of the elements. The atomic percentages of C, O, and Ag were observed to be 91.56%, 6.44%, and 2.01%, respectively. We selected PCL for its mechanical strength, β-CD for high bacterial entrapment, and $AgNO_3$ as the antibacterial agent.[16−18] We hypothesized that parallel nanofibers of PCL can provide a more consistent bacterial adhesion.[19] The β-CD can retain most bacterial cells owing to the unique hydrophobic cavity-mediated host−guest interaction that traps several bacteria, such as *Escherichia coli*, *Staphylococcus epidermidis*, *Pseudomonas aeruginosa*, *Bacillus subtilis*, *Klebsiella pneumonia*.[20−26] While $AgNO_3$ is for photoreduction and photocatalytic production of ROS and antimicrobial activity. Silver's heat conductivity, sunlight absorption, and nanoparticle synthesis efficiency make it more effective than copper and iron in photocatalytic antimicrobial applications.[27−29]

Next, we electrospun the middle PM layer of randomly arranged conductive mat with an interfiber spacing of ≥1 μm. We chose to incorporate larger interfiber spacing to enhance airflow, which helps maintain a more breathable environment along with electrically induced bacterial killing.[30]

As observed in the SEM images, the PM fibers were loosely interwoven creating a substantial amount of space in 3D. The average diameter of these nanofibers was measured to be 0.292 ± 0.01 μm. The fibers, therefore, had a much thinner diameter compared to the PBA nanofibers. The uniform distribution of the elements was observed in the SEM-EDX. The atomic percentage distribution of C, O, and N were observed to be 90.93%, 7.86%, and 1.21%, respectively (Figure 1b, middle panel). We intend to use the conductive property of the MWCNT to achieve electrical field-induced disruption of any bacterial species, thus giving the mask self-sterilization ability against broader bacterial species. Besides, MWCNT incorporated within a PVA matrix reduces the local inflammatory effect on human skin through a barrier effect.[31]

We designed the innermost layer PCC layer which comes in direct contact with the skin, using highly biocompatible biomaterials capable of absorbing moisture and preventing the buildup of water from exhaled air. The layer components (PVA, CMC, and CNF) are all hydrophilic.[32−34] We designed the PCC layer with fibers having a similar fiber diameter to the PM layer, however with reduced interfiber spacing. The average diameter observed for this nanofiber was 0.270 ± 5 μm. A lower magnification image shows densely packed random nanofibers with sparse interfiber spacing compared to the middle PM layer. A uniform distribution of the elements was observed in the SEM-EDX. The atomic percentage of C, O, and S were 87.98%, 11.63%, and 0.39%, respectively (Figure 1b, lower panel). Thus, the microstructure of the fabricated mask fiber consisted of an outer layer of parallelly arranged nanofibers and a middle and inner layer of randomly arranged nanofibers. All three layers were electrospun on a medical

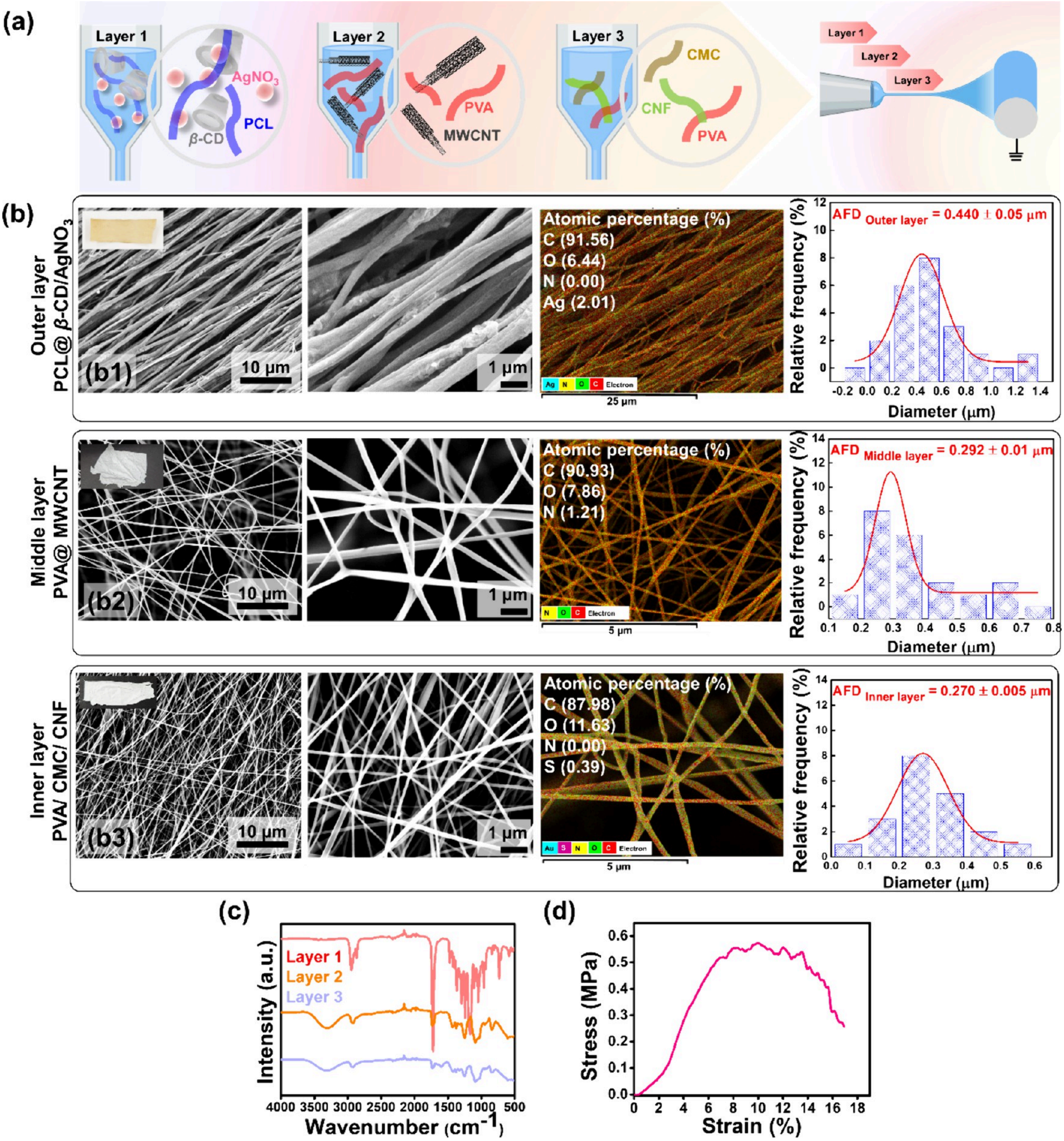

Figure 1. Fabrication and morphological characterization of the fabricated nanofibers. (a) Schematic illustration of the fabrication steps and the components of the nanofiber layers. (b) The FE-SEM images of the electrospun layers including the outer PBA layer (upper panel), middle PM layer (middle panel), and the innermost PCC layer (lower panel) along with their corresponding EDX and fiber size distribution. (c) The FTIR spectra of the three layers of the fabricated mask. (d) Tensile stress−strain graph of the trilayered electrospun fiber mat. AFD: average fiber diameter.

gauge, restricting the mask thickness to 0.36 mm, compared to ∼0.79 mm for a commercially available surgical mask.

Next, we analyzed the chemical environment in the nanofibers through the FTIR analysis. The FTIR spectra of each layer indicated the abundance of distinct functional groups (Figure 1c). In the PBA layer, we observed peaks at 2500−3000 $\mathrm{cm^{-1}}$ compared to the PM and the PCC layers, indicating the presence of C−H stretching of alkyne or aldehyde groups. The sharp peak at approximately 1700 $\mathrm{cm^{-1}}$ indicated the presence of strong C═O (carbonyl) stretching, while the appearance of peaks between 500 and 1500 $\mathrm{cm^{-1}}$ showed the abundance of functional groups including O−H (hydroxyl), C−H (Methyl), C−O (Carbonyl), C−O−C (Ester or ether) stretching, and C═C bonds. The combination

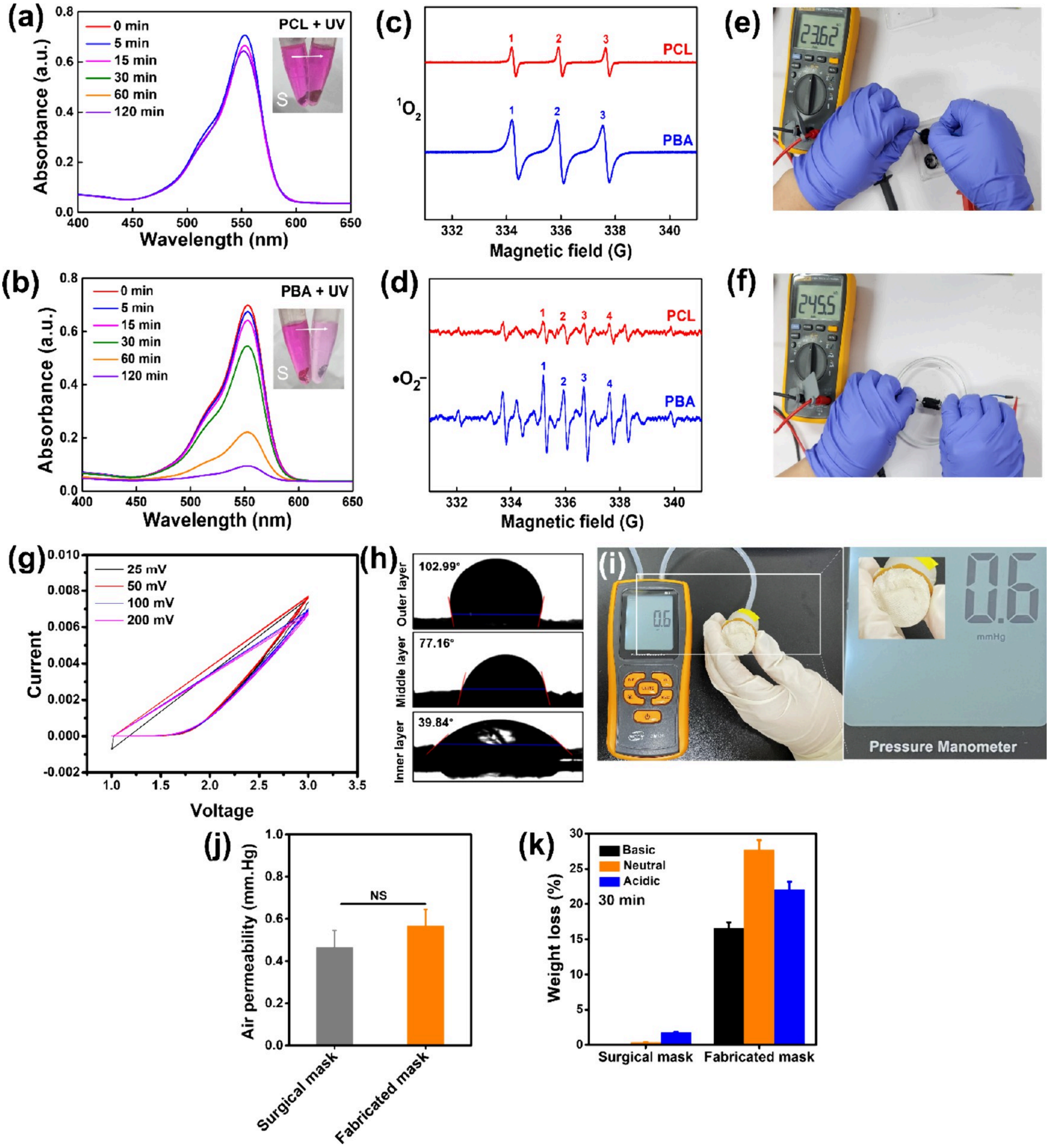

Figure 2. Functional characterizations of the fabricated nanofiber layers. (**a**−**d**) Photocatalytic activity of the PCL nanofiber and the outer PBA layer in the presence of UV exposure. (**a, b**) RhB degradation in the presence of PCL and PBA fibers exposed to UV irradiation. S: sample. (**c**) A three-line spectrum with an intensity ratio of 1:1:1 formed by TEMP, demonstrating the ability of the PBA layer to activate H_2O_2 and produce $^1O_2$. (**d**) A four-line spectra with an intensity ratio of 1:1:1:1 in the presence of DMPO showing the generation of $^•O_2^-$; (**e**−**g**) Conductivity test of the middle PM layer. (**e, f**) Digital images of the digital multimeter indicating the measured resistance of the PM hydrogel (**e**) and PM nanofiber layer (**f**) along with the respective oxidation−reduction cycles observed for PM layer in cyclic voltammetry (**g**). (**h**) Contact angle measurements of the inner PCC layer compared to the outer and middle layers showing the moisture absorption ability of the inner layer. (**i, j**) Air permeability test of the trilayered nanofiber mask. (**k**) Biodegradability assessment of the fabricated layers under basic, neutral, and acidic environments compared to that of a surgical mask.

of these functional groups suggests that the outer layer will not only facilitate enhanced interaction with bacterial cells but also possess intrinsic antibacterial properties. These functional groups are known to interact with bacterial cells through various chemical mechanisms, including membrane disruption and oxidative damage. In the case of the PM nanofiber layer, we observed a peak at ~3375 cm^{-1}, indicating the presence of O−H stretching. The peak at ~2951 cm^{-1} indicates asymmetric −CH_2 stretching vibration, while the peak at ~1690 cm^{-1} indicates the presence of C═O stretching. The presence of these functional groups is expected to contribute to the direct chemical disruption of the bacterial cells, while conductivity can enhance this effect through the electrochemical process. The FTIR spectra of the PCC layer showed the vibration of C−O at ~1063 cm^{-1}, −C═O at ~1430 cm^{-1}, and N−H bending at ~1595 cm^{-1}. In addition, a stretching vibration of the −OH group is observed at ~3400 cm^{-1}. The abundance of CO, C═O, NH, and OH is expected to increase the hydrophilicity of the nanofibers, enhancing their moisture retention ability and biocompatibility. The abundance of specific functional groups in different layers of the face mask is expected to favor bacterial attachment and increase the antibacterial property while improving moisture-absorbing ability.[35,36]

The fabricated trilayered electrospun layers (combined three layers) were then tested for their mechanical properties, according to the universal testing machine (UTM) measurement standard. The fabricated mask was subjected to mechanical strain, and the breakpoint stress was calculated. We observed a breakpoint stress of ~0.5 MPa, as shown in Figure 1d. This value indicates the softness, lightweight nature, and flexibility of the trilayered electrospun mat.[37,38]

Next, we evaluated the unique chemical characteristics of each layer of the fabricated mask as depicted in Figure 2. First, we tested the photocatalytic activity of the PBA layer in the presence of UV using the Rhodamine B (RhB) degradation method. As indicated in Figures 2a, and 2b, a decrease in the UV spectra (at 550 nm) of RhB was observed for PBA compared to PCL over 120 min. The corresponding photographic images of the discoloration of RhB in the presence of PBA are given in the insets of Figures 2a and 2b. During photocatalytic degradation, RhB loses its color as ROS generated by the photocatalyst attack, breaking down the dye′s conjugated chromophoric structure. This process reduces the dye′s ability to absorb visible light, resulting in a noticeable decrease in color intensity.[39] Thus, this discoloration and the reduction of the absorbance in the presence of PBA indicates the photocatalytic activity of the PBA layer. We further determined the production of ROS in the samples through EPR spectroscopy.

The characteristic EPR signal of the nitroxyl radical TEMPO was observed in PBA, which is formed by the reaction of TEMP with $^1O_2$ (Figure 2c). The formation of oxygen radical ($^\bullet O_2^-$) was recorded upon infrared irradiation in the case of PBA, as shown in Figure 2d. The photocatalytic ability of the PBA layer is crucial for the antibacterial efficiency of the fabricated face mask. Next, we tested the conductivity of the PM layer in sheet and gel form. A resistance of 23.62 kΩ was recorded for the PM hydrogel (Figure 2e), compared to 245.5 kΩ for the PM layer (Figure 2f), indicating that the presence of water contributes to the higher electrical conductivity in the gel form. Further, the PM layer was observed to show oxidation−reduction properties as studied through the cyclic voltammetry analysis (Figure 2g). The cyclic voltammogram exhibited a distinctive oval shape instead of the sharp, well-developed oxidation and reduction peaks typically observed. This broad, rounded feature suggests that the redox processes occurring within the gel are likely irreversible or quasi-reversible.[40] The oval shape of the voltammogram may indicate slower electron transfer kinetics or the influence of the gel matrix on the electrochemical reactions. Additionally, the peaks could be affected by the interaction between the PVA and MWCNT components, or by overlapping redox processes within the gel.[41−43]

The fabricated fibers were then tested for their water absorption ability. An equal amount of water was placed on each fiber surface, and the absorption was recorded (Figure 2h). The contact angle measured for the outer layer was 102.99°, for the middle layer 77.16°, and for the inner layer 39.84°, indicating increased hydrophilicity in the PCC layer.

The PBA layer exhibiting a contact angle of 102.99° shows its high resistance to wetting by water, as indicated by the large contact angle where water droplets bead up rather than spread across the surface. This hydrophobicity arises from the nonpolar, hydrophobic aliphatic chains of PCL that repel water. The PM layer exhibits a water contact angle of 77.16° due to the hydrophilic nature of PVA, which rapidly interacts with water owing to its numerous hydroxyl (−OH) groups. The inclusion of typically hydrophobic MWCNTs slightly decreases the overall hydrophilicity. However, the hydrophilic components of the PCC layer reduce its contact angle to 39.84°. CNFs are known to have abundant −OH groups, which form hydrogen bonds with water, enhancing water affinity.[44] Carboxymethyl chitosan′s C═O and −OH groups increase the composite′s hydrophilicity by attracting and bonding with water.[45,46] While, PVA adds extra hydroxyl groups, making the PCC layer more hydrophilic.[47] The PCC layer exhibits a low contact angle, suggesting that water spreads easily across its surface, thereby increasing its moisture absorption capacity. Therefore, the inner layer is anticipated to absorb moisture from the breath effectively.

We next evaluated the air permeability efficiency of the mask. Figure 2i displays the air permeability values of the fabricated mask measured through a custom-built blower connected to a manometer. A 0.6 mmHg pressure was recorded when air was blown through the mask. The air permeability through the fabricated mask and surgical mask was similarly recorded and the values are plotted in Figure 2j. The manometer reading of 0.6 mmHg when air is forced through the mask indicates moderate to high air permeability efficiency. The relatively small pressure differential suggests that air flows through the mat with little resistance, indicating a porous structure that facilitates smooth airflow.[48] The mask′s excellent air permeability and structural integrity make it ideal for use.

We evaluated the mask′s degradation in acidic, basic, and neutral conditions. The fabricated mask degraded faster than a commercial surgical mask. As shown in Figure 2k, the weight loss ranged from 15% to 30% within 30 min of treatment. The highest degradability was observed in a neutral environment (~27%), followed by acidic (~20%) and the basic treatments (~16%). The fabricated mask is engineered to optimize degradation under neutral pH conditions, aligning with typical use environments. The observed lower degradation rates in acidic and basic environments suggest that while the mask adapts to varying pH levels, its material composition offers greater resistance to extreme pH conditions, potentially delaying the biodegradation process. These properties highlight the mask′s suitability for standard healthcare applications, where neutral pH is prevalent, and its potential to contribute to sustainability by reducing environmental impact.

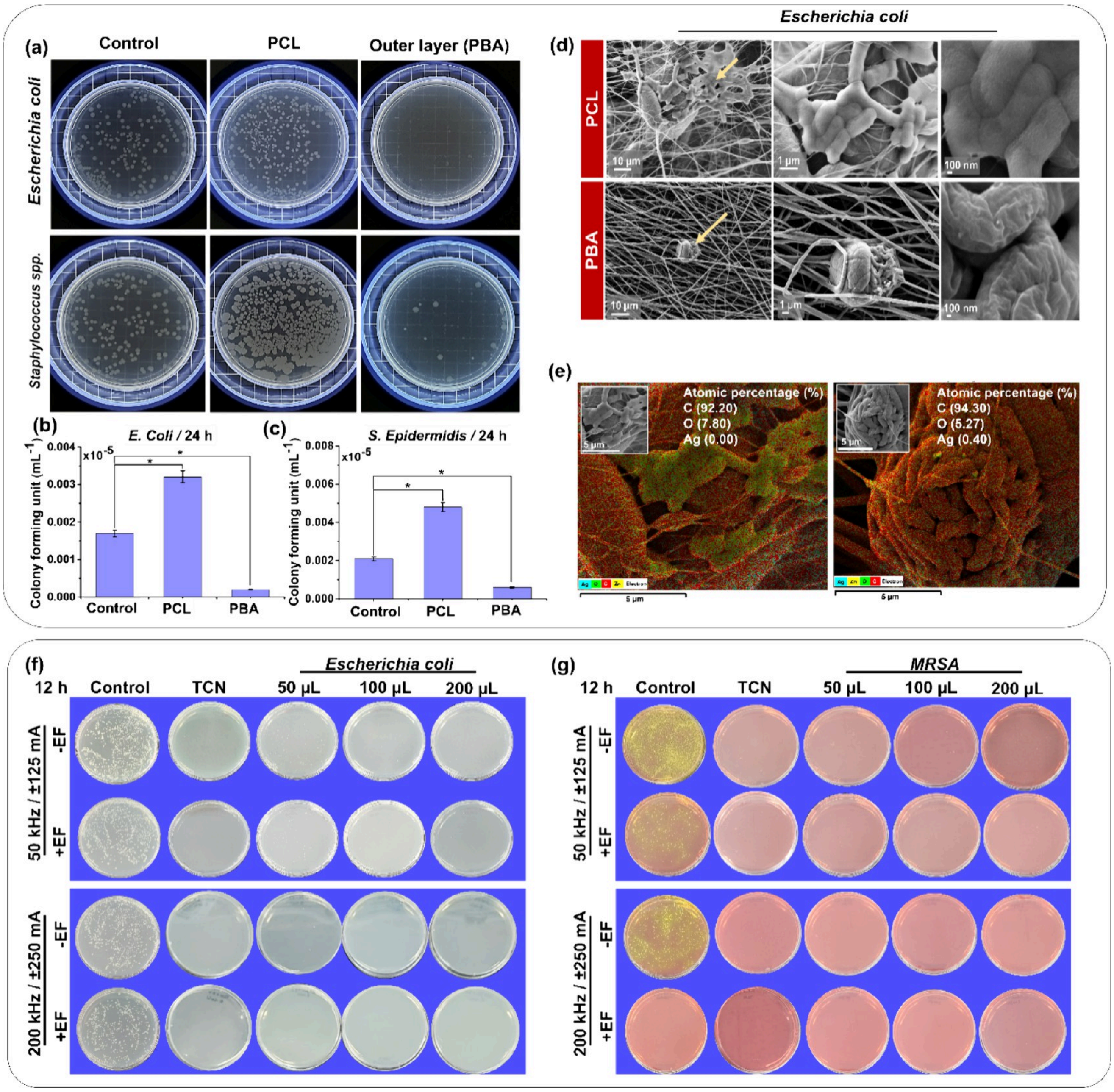

Figure 3. Antibacterial test of the PBA and the PM layers against Gram-positive and Gram-negative bacteria. (**a**) Plate assay showing the antibacterial property of the PBA layer with the corresponding (**b, c**) colony forming units. (**d**) FE-SEM images of *E. coli* showing cell wall corrugation in the PBA layer with respect to PCL control along with (**e**) the corresponding elemental composition in the scanned area indicating the presence of Ag. (**f**) The antibacterial efficiency of the middle PM layer against *E. coli* at various bacterial concentrations in the absence or presence of electrical stimulation. (**g**) The antibacterial efficiency of the middle PM layer against MRSA at various bacterial concentrations in the absence or presence of ES.

Next, we analyzed the antibacterial efficiency of the mask. As shown in Figure 3, the PBA layer demonstrated high antibacterial activity against *E. coli*, *Staphylococcus epidermidis* (*S. epidermidis*), and Methicillin-resistant *Staphylococcus aureus* (MRSA), with colony-forming units less than 0.001 (Figure 3a-c and Supporting Information S2). This remarkably low CFU count indicates that the material is highly effective against both Gram-negative (*E. coli*) and Gram-positive (*S. epidermidis* and MRSA) bacteria, suggesting its potent broad-spectrum antimicrobial activity.

AgNPs are well-known to damage bacteria through many mechanisms including cell structural disruption. We, therefore, evaluated the probable damaging effect of PBA on the bacterial cells through the SEM images of the *E. coli* culture. *E. coli* was chosen for studying the cell wall disruption and morphological damage due to its cell wall structure, which is more accessible for observation compared to the Gram-positive thicker peptidoglycan layer.[49] We observed severe surface corrugation in *E. coli* (Figure 3d). The atomic percentage of Ag in the scanned area was 0.40% (Figure 3e).

The PBA-incubated *E. coli* and MRSA were further exposed to sunlight, and the UV spectra were recorded to observe the formation of silver nanoparticles (Supporting Information S3).

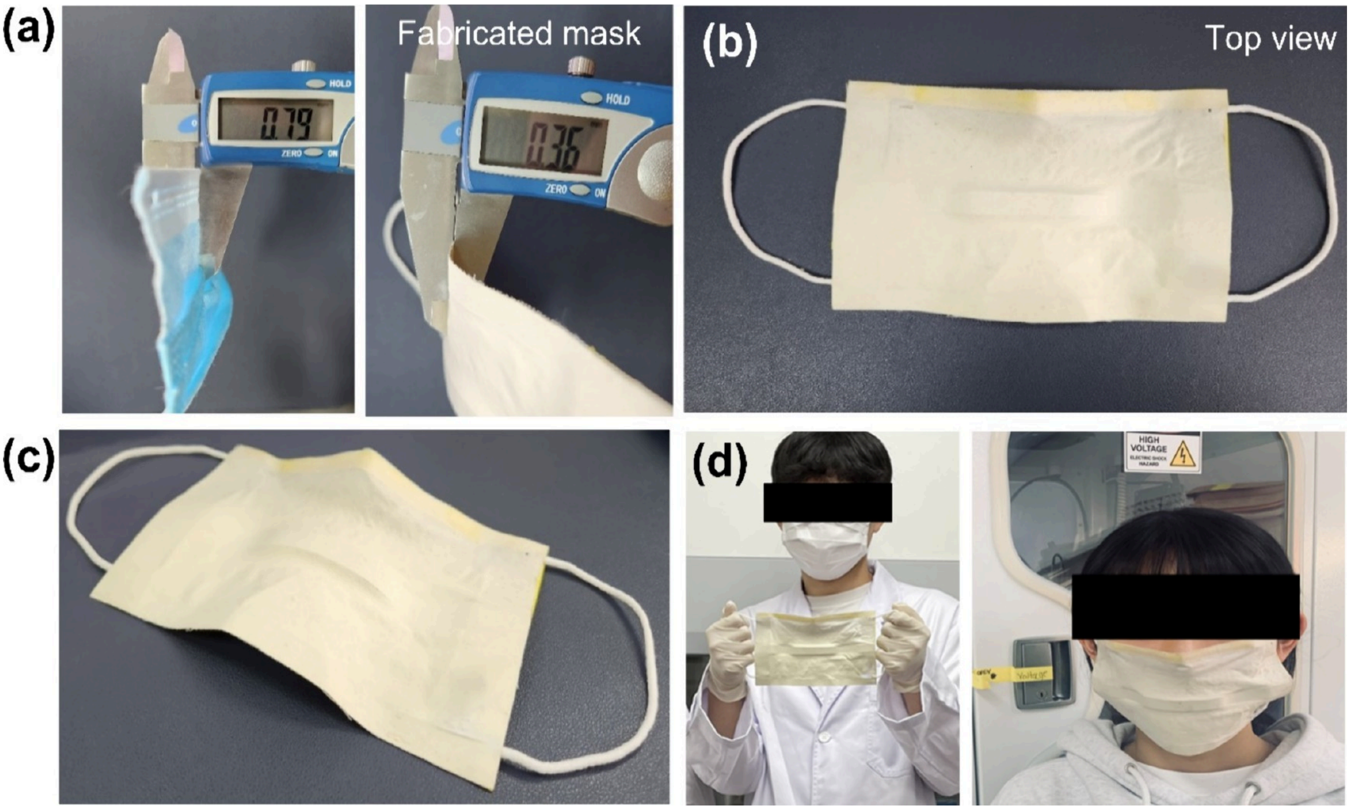

[redacted]

[redacted]

Figure 4. Visual comparison and demonstration of the fabricated mask. **(a)** Thickness comparison between commercially available and trilayered face mask. **(b, c)** Digital top view of the trilayered face mask, illustrating its layered structure and compact design. **(d)** Fabricated mask worn by an individual, reflecting its comfortable fit, effective coverage, and potential for daily wear.

The photochemical reaction of $AgNO_3$ in the presence of sunlight was confirmed by the color change of the bacterial suspension (from colorless to brown) in the presence of PBA. The PBA film displays enhanced antimicrobial activity due to sunlight-induced reduction of Ag^+ ions to AgNPs, which damage bacterial cells through heat distribution and ROS generation, as confirmed by TEMPO-mediated detection.

We then evaluated the antibacterial efficacy of the conductive PM layer under low (50 kHz/ ± 125 mV) and high (200 kHz/±250 mV) electrical stimulation (ES). The PM layer was observed to be antibacterial at both examined ES against both types of bacteria (Figure 3f,g). The corresponding colony-forming units and OD values of *E. coli* and MRSA showed similar trends, indicating the electricity-induced antibacterial efficiency of the PM layer and its electricity-induced self-cleaning ability (Supporting Information S4 (a-d) and S5 (a-d)). We further checked the self-cleaning ability of the PM layer against *S. epidermidis*. A similar trend was observed in *S. epidermidis* growth under 50 kHz/ ± 125 mV (Supporting Information S6 (a-c)), confirming the antibacterial efficiency of the PM layer.

The fabricated prototype mask was compared for its usability with commercially available surgical masks (Figure 4). The thickness of our mask was 0.36 mm compared to 0.79 mm of the surgical mask (Figure 4a-d). This reduced thickness, while maintaining antibacterial efficacy, offers advantages in air permeability, comfort, reduced fogging, and potential cost-effectiveness.

Next, we evaluated the longevity of the mask under multiple aqueous washes with/without ES, and exposure to different temperatures. The mask retained antibacterial properties after the first two washes without ES (Supporting Information S7a-d), while, no bacterial colonies following the third wash, appeared with ES, demonstrating sustained antibacterial efficacy. The OD (Supporting Information S7e) and CFU estimation (Supporting Information S7f-h) further confirmed the retained antibacterial efficiency upon ES. These results indicate that ES sterilizes the mask better than washing. Washing reduced the breakpoint stress to 0.63 MPa w.r.t. 0.8 MPa for the unwashed mask, indicating material degradation or aging (Supporting Information S7i-j).

We further assessed the antibacterial property of the mask upon exposure to controlled temperatures of 45 °C and −20 °C. As indicated in Supporting Information S8a, b, the mask retained its antibacterial effect postexposure to the indicated temperatures. However, upon exposure to −20 °C, few bacterial colonies began to emerge as confirmed CFU count and OD (Supporting Information S8c-f), suggesting a stable antibacterial performance at moderate and elevated temperatures.

We further evaluated the biocompatibility of the nanofibers by assessing cell viability and actin organization in human dermal fibroblasts (HDF) and human keratinocytes (HaCaT) cells. As shown in the live/dead analysis in Supporting Information S9a, all three fiber layers were compatible with the HDF over 7 and 14 days of incubation (Supporting Information S9b). Moreover, the percentage of cell viability was higher than the control on days 5 and 7 postincubation. A similar trend was observed in HaCaT cells, where no toxicity was recorded in the live/dead analysis. Additionally, the percentage of cell viability was higher in the nanofiber-treated cells (Supporting Information S10a, b). Next, we examined the actin organization in HDF and HaCaT cells after 5 days of incubation (Supporting Information S11a). We observed no aberrant actin filament in any cells. The PM layer had the greatest correlated total cell fluorescence (CTCF) in both cell lines (Supporting Information S11 b, c).

Herein, we developed a novel face mask prototype designed to improve both user comfort and filtration efficiency. This innovation provides improved defense against airborne diseases by incorporating biodegradable polymers, antibacterial compounds, and self-cleaning materials into a micro/nanofibrous framework. Additionally, it minimizes environmental impact. Final development is required to refine the electrospun mask design according to American Society for Testing and Materials (ASTM) standards to ensure its suitability for commercial production. Moreover, the mask requires enhancement in aesthetics and size fitting to improve customer satisfaction.

ASSOCIATED CONTENT

Supporting Information

The Supporting Information is available free of charge at https://pubs.acs.org/doi/10.1021/acs.nanolett.4c04525.

> FE-SEM images of electrospun PCL, antibacterial test of the PBA layer, catalytic activity of the PBA layer, photoreduction of $AgNO_3$, antibacterial test of the PM layer against *E. coli*, MRSA, and *S. epidermidis* under ES, longevity test and biocompatibility assessment of the mask (PDF)

AUTHOR INFORMATION

Corresponding Authors

Beom-Soo Shin − *Department of Biosystems Engineering, Kangwon National University, Chuncheon 24341, Republic of Korea; Interdisciplinary Program in Smart Agriculture, Kangwon National University, Chuncheon 24341, Republic of Korea*; Email: bshin@kangwon.ac.kr

Dae Hyun Kim − *Department of Biosystems Engineering, Kangwon National University, Chuncheon 24341, Republic of Korea; Interdisciplinary Program in Smart Agriculture, Kangwon National University, Chuncheon 24341, Republic of Korea*; Email: daekim@kangwon.ac.kr

Ki-Taek Lim − *Department of Biosystems Engineering, Kangwon National University, Chuncheon 24341, Republic of Korea; Interdisciplinary Program in Smart Agriculture, Kangwon National University, Chuncheon 24341, Republic of Korea*; orcid.org/0000-0003-2091-788X; Email: ktlim@kangwon.ac.kr

Authors

Keya Ganguly − *Department of Biosystems Engineering, Kangwon National University, Chuncheon 24341, Republic of Korea; Department of Mechanical Engineering, Virginia Tech, Blacksburg, Virginia 24061, United States*

Aayushi Randhawa − *Department of Biosystems Engineering, Kangwon National University, Chuncheon 24341, Republic of Korea; Interdisciplinary Program in Smart Agriculture, Kangwon National University, Chuncheon 24341, Republic of Korea*

Sayan Deb Dutta − *Department of Biosystems Engineering, Kangwon National University, Chuncheon 24341, Republic of Korea*; orcid.org/0000-0001-9397-3140

Hyeonseo Park − *Department of Biosystems Engineering, Kangwon National University, Chuncheon 24341, Republic of Korea*

Mehran Mohammad Hossein Pour − *Department of Mechanical Engineering, Virginia Tech, Blacksburg, Virginia 24061, United States*

Hojin Kim − *Department of Biosystems Engineering, Kangwon National University, Chuncheon 24341, Republic of Korea; Department of Mechanical Engineering, Virginia Tech, Blacksburg, Virginia 24061, United States; Interdisciplinary Program in Smart Agriculture, Kangwon National University, Chuncheon 24341, Republic of Korea*

Rumi Acharya − *Department of Biosystems Engineering, Kangwon National University, Chuncheon 24341, Republic of Korea; Department of Mechanical Engineering, Virginia Tech, Blacksburg, Virginia 24061, United States; Interdisciplinary Program in Smart Agriculture, Kangwon National University, Chuncheon 24341, Republic of Korea*

Tejal V. Patil − *Department of Biosystems Engineering, Kangwon National University, Chuncheon 24341, Republic of Korea; Department of Mechanical Engineering, Virginia Tech, Blacksburg, Virginia 24061, United States; Interdisciplinary Program in Smart Agriculture, Kangwon National University, Chuncheon 24341, Republic of Korea*

Complete contact information is available at: https://pubs.acs.org/10.1021/acs.nanolett.4c04525

Author Contributions

K.G. and A.R. have contributed equally to the manuscript.

Notes

The authors declare no competing financial interest.

ACKNOWLEDGMENTS

This study was supported by the 'Basic Science Research Program' through the 'National Research Foundation of Korea' funded by the 'Ministry of Education' (NRF-2018R1A16A1-A03025582 and NRF2022R1I1A3063302). This research was supported by the MSIT (Ministry of Science and ICT), Korea, under the Innovative Human Resource Development for Local Intellectualization support program (IITP- (IITP-2024-RS-2023-00260267) supervised by the IITP (Institute for Information & Communications Technology Planning & Evaluation).

REFERENCES

(1) Zhang, H.; Li, X.; Ma, R.; Li, X.; Zhou, Y.; Dong, H.; Li, X.; Li, Q.; Zhang, M.; Liu, Z.; Wei, B.; Cui, M.; Wang, H.; Gao, J.; Yang, H.; Hou, P.; Miao, Z.; Chai, T. Airborne Spread and Infection of a Novel Swine-Origin Influenza A (H1N1) Virus. *Virol J.* **2013**, *10*, DOI: 10.1186/1743-422X-10-204.

(2) Tang, C. Y.; Ramesh, A.; Wan, X.-F. Avian and Swine Influenza Viruses. *Molecular Medical Microbiology, Third Edition* **2024**, 2375−2411.

(3) Bowdle, A.; Brosseau, L. M.; Tellier, R.; MacIntyre, C. R.; Edwards, M.; Jelacic, S. Reducing Airborne Transmissible Diseases in Perioperative Environments. *Br J. Anaesth* **2024**, *133* (1), 19−23.

(4) Murdoch, D. R.; Werno, A. M.; Jennings, L. C. Microbiological Diagnosis of Respiratory Illness: Recent Advances. *Kendig's Disorders of the Respiratory Tract in Children (Ninth Edition)* **2019**, 396−405.

(5) Herman, E. K.; Lacoste, S. R.; Freeman, C. N.; Otto, S. J. G.; McCarthy, E. L.; Links, M. G.; Stothard, P.; Waldner, C. L. Bacterial Enrichment Prior to Third-Generation Metagenomic Sequencing Improves Detection of BRD Pathogens and Genetic Determinants of

Antimicrobial Resistance in Feedlot Cattle, *Front Microbiol* **2024**, *15*, DOI: 10.3389/fmicb.2024.1386319.

(6) Ralhan, K.; Iyer, K. A.; Diaz, L. L.; Bird, R.; Maind, A.; Zhou, Q. A. Navigating Antibacterial Frontiers: A Panoramic Exploration of Antibacterial Landscapes, Resistance Mechanisms, and Emerging Therapeutic Strategies. *ACS Infectious Diseases* **2024**, 1483−1519, DOI: 10.1021/acsinfecdis.4c00115.

(7) Wei, Y.; Fan, X.; Chen, D.; Zhu, X.; Yao, L.; Zhao, X.; Tang, X.; Wang, J.; Zhang, Y.; Qiu, T.; Hao, Q. Probing Oxidation Mechanisms in Plasmonic Catalysis: Unraveling the Role of Reactive Oxygen Species. *Nano Lett.* **2024**, *24* (6), 2110−2117.

(8) Zhao, T.; Xu, Y.; Wu, M.; Li, Y.; Ma, J.; Li, H.; Zheng, Y.; Zeng, Y. Highly Efficient Fabrication of Biomimetic Nanoscaled Tendrils for High-Performance PM0.3 Air Filters. *Nano Lett.* **2024**, *24* (4), 1385−1391.

(9) Yang, M.; Gong, X.; Wang, S.; Tian, Y.; Yin, X.; Wang, X.; Yu, J.; Zhang, S.; Ding, B. Two-Dimensional Nanofibrous Networks by Superspreading-Based Phase Inversion for High-Efficiency Separation. *Nano Lett.* **2023**, *23* (22), 10579−10586.

(10) Han, S.; Kim, J.; Lee, Y.; Bang, J.; Kim, C. G.; Choi, J.; Min, J.; Ha, I.; Yoon, Y.; Yun, C. H.; Cruz, M.; Wiley, B. J.; Ko, S. H. Transparent Air Filters with Active Thermal Sterilization. *Nano Lett.* **2022**, *22* (1), 524−532.

(11) Kumar, S.; Karmacharya, M.; Joshi, S. R.; Gulenko, O.; Park, J.; Kim, G. H.; Cho, Y. K. Photoactive Antiviral Face Mask with Self-Sterilization and Reusability. *Nano Lett.* **2021**, *21* (1), 337−343.

(12) Ma, X.; Wu, D.; Wang, J.; Sun, F.; Li, Z.; Zhang, L.; Xiao, Y. Make the Invisible Visible: Valuation of the Hidden Cost of Particulate-Filtering Facemask Use against Air Pollution in China, *J. Clean Prod* **2022**, *372*, 133667.

(13) Pandit, P.; Maity, S.; Singha, K.; Annu; Uzun, M.; Shekh, M.; Ahmed, S. Potential Biodegradable Face Mask to Counter Environmental Impact of Covid-19. *Cleaner Engineering and Technology* **2021**, DOI: 10.1016/j.clet.2021.100218.

(14) Oliveira, A. M.; Patrício Silva, A. L.; Soares, A. M. V. M.; Barceló, D.; Duarte, A. C.; Rocha-Santos, T. Current Knowledge on the Presence, Biodegradation, and Toxicity of Discarded Face Masks in the Environment, *J. Environ. Chem. Eng.* **2023**, *11* (2), 109308.

(15) Nilashi, M.; Ali Abumalloh, R.; Ahmadi, H.; Alrizq, M.; Alghamdi, A.; Alghamdi, O. A.; Alyami, S. A Proposed Method for Quality Evaluation of COVID-19 Reusable Face Mask. *Measurement and Control (United Kingdom)* **2024**, *57* (6), 828−840.

(16) Sawadkar, P.; Mohanakrishnan, J.; Rajasekar, P.; Rahmani, B.; Kohli, N.; Bozec, L.; García-Gareta, E. A Synergistic Relationship between Polycaprolactone and Natural Polymers Enhances the Physical Properties and Biological Activity of Scaffolds. *ACS Appl. Mater. Interfaces* **2020**, *12* (12), 13587−13597.

(17) Saha, P.; Rafe, M. R. Cyclodextrin: A Prospective Nanocarrier for the Delivery of Antibacterial Agents against Bacteria That Are Resistant to Antibiotics. *Heliyon* **2023**, DOI: 10.1016/j.heliyon.2023.e19287.

(18) Ribeiro, A. I.; Dias, A. M.; Zille, A. Synergistic Effects between Metal Nanoparticles and Commercial Antimicrobial Agents: A Review. *ACS Applied Nano Materials* 2022, 3030−3064, DOI: 10.1021/acsanm.1c03891.

(19) Dawson, C.; Xu, F.; Hoare, T. Reactive Cell Electrospinning of Anisotropically Aligned and Bilayer Hydrogel Nanofiber Networks. *ACS Biomater Sci. Eng.* **2023**, *9* (11), 6490−6503.

(20) Benchallal, F.; Belkacemi, H.; Bellil, Z.; Chebrouk, F.; Touati, A. Thymus Vulgaris Essential Oil Enclosed in β-Cyclodextrin as Drug Delivery System: A Promising Alternative for Antibiotic Usage in Combating Salmonella. *Proceedings of the Indian National Science Academy* **2024**, *90*, 1095.

(21) Akinola, O. T.; Oyebamiji, A. K.; Oke, D. G.; Adekunle, D. O.; Olanrewaju, A. A.; Akintelu, S. A. In Silico Analysis on Binding Action of Beta-Lactam Drugs against TEM and SHV Class A Beta-Lactamases from Klebsiella Pneumoniae, *Discover Applied Sciences* **2024**, *6* (4), DOI: 10.1007/s42452-024-05783-8.

(22) Gurung, P.; Das, A.; Pradhan, S.; Chettri, A.; Dutta, T.; Sinha, B. A New Amino Functionalized Thio-Modified β-Cyclodextrin Based Ligand and Its Fe(III) Complex with Physico-chemical and Antibacterial Activity: An Integrated Experimental and Computational Investigation. *J. Incl Phenom Macrocycl Chem.* **2024**, *104*, 461.

(23) Wankar, J.; Kotla, N. G.; Gera, S.; Rasala, S.; Pandit, A.; Rochev, Y. A. Recent Advances in Host-Guest Self-Assembled Cyclodextrin Carriers: Implications for Responsive Drug Delivery and Biomedical Engineering. *Advanced Functional Materials.* **2020**, DOI: 10.1002/adfm.201909049.

(24) Rouillard, K. R.; Markovetz, M. R.; Bacudio, L. G.; Hill, D. B.; Schoenfisch, M. H. Pseudomonas Aeruginosa Biofilm Eradication via Nitric Oxide-Releasing Cyclodextrins. *ACS Infect Dis* **2020**, *6* (7), 1940−1950.

(25) Zhan, W.; Xu, L.; Liu, Z.; Liu, X.; Gao, G.; Xia, T.; Cheng, X.; Sun, X.; Wu, F. G.; Yu, Q.; Liang, G. Tandem Guest-Host-Receptor Recognitions Precisely Guide Ciprofloxacin to Eliminate Intracellular Staphylococcus Aureus, *Angewandte Chemie - International Edition* **2023**, *62* (32), DOI: 10.1002/anie.202306427.

(26) Perez-Anes, A.; Szarpak-Jankowska, A.; Jary, D.; Auzély-Velty, R. β-CD-Functionalized Microdevice for Rapid Capture and Release of Bacteria. *ACS Appl. Mater. Interfaces* **2017**, *9* (16), 13928−13938.

(27) Dakal, T. C.; Kumar, A.; Majumdar, R. S.; Yadav, V. Mechanistic Basis of Antimicrobial Actions of Silver Nanoparticles. *Front Microbiol* **2016**, *7* (NOV), DOI: 10.3389/fmicb.2016.01831.

(28) Yin, Y.; Liu, J.; Jiang, G. Sunlight-Induced Reduction of Ionic Ag and Au to Metallic Nanoparticles by Dissolved Organic Matter. *ACS Nano* **2012**, *6* (9), 7910−7919.

(29) Chakraborty, S.; Sagarika, P.; Rai, S.; Sahi, C.; Mukherjee, S. Tyrosine-Templated Dual-Component Silver Nanomaterials Exhibit Photoluminescence and Versatile Antimicrobial Properties through ROS Generation. *ACS Appl. Mater. Interfaces* **2021**, *13* (31), 36938−36947.

(30) Wei, Z.; Su, Q.; Wang, X.; Long, S.; Zhang, G.; Lin, Q.; Yang, J. Nanofiber Air Filters with High-Temperature Stability and Superior Chemical Resistance for the High-Efficiency PM2.5 Removal. *Ind. Eng. Chem. Res.* **2021**, *60* (27), 9971−9982.

(31) Zarei, M.; Lee, G.; Lee, S. G.; Cho, K. Advances in Biodegradable Electronic Skin: Material Progress and Recent Applications in Sensing, Robotics, and Human-Machine Interfaces. *Adv. Mater.* **2023**, DOI: 10.1002/adma.202203193.

(32) Yoon, J.; Zhang, X.; Ryu, M.; Kim, W. H.; Ihm, K.; Lee, J. W.; Li, W.; Lee, H. Tailoring the Hydrophilicity for Delayed Condensation Frosting in Antifogging Coatings. *ACS Appl. Mater. Interfaces* **2022**, *14* (30), 35064−35073.

(33) Li, M.; Li, J.; Zhou, M.; Xian, Y.; Shui, Y.; Wu, M.; Yao, Y. Super-Hydrophilic Electrospun PVDF/PVA-Blended Nanofiber Membrane for Microfiltration with Ultrahigh Water Flux. *J. Appl. Polym. Sci.* **2020**, *137* (9), DOI: 10.1002/app.48416.

(34) Niu, P.; Mao, H.; Lim, K. H.; Wang, Q.; Wang, W. J.; Yang, X. Nanocellulose-Based Hollow Fibers for Advanced Water and Moisture Management. *ACS Nano* **2023**, *17* (15), 14686−14694.

(35) Yu, Q.; Wu, Z.; Chen, H. Dual-Function Antibacterial Surfaces for Biomedical Applications. *Acta Biomaterialia.* **2015**; 1−13. DOI: 10.1016/j.actbio.2015.01.018.

(36) Hamdan, N.; Yamin, A.; Hamid, S. A.; Khodir, W. K. W. A.; Guarino, V. Functionalized Antimicrobial Nanofibers: Design Criteria and Recent Advances. *Journal of Functional Biomaterials.* **2021**, DOI: 10.3390/jfb12040059.

(37) Luo, Z.; Chen, J.; Zhu, Z.; Li, L.; Su, Y.; Tang, W.; Omisore, O. M.; Wang, L.; Li, H. High-Resolution and High-Sensitivity Flexible Capacitive Pressure Sensors Enhanced by a Transferable Electrode Array and a Micropillar-PVDF Film. *ACS Appl. Mater. Interfaces* **2021**, *13* (6), 7635−7649.

(38) Zhang, Q.; Wang, Q.; Wang, G.; Zhang, Z.; Xia, S.; Gao, G. Ultrathin and Highly Tough Hydrogel Films for Multifunctional Strain Sensors. *ACS Appl. Mater. Interfaces* **2021**, *13* (42), 50411−50421.

(39) Yu, K.; Yang, S.; He, H.; Sun, C.; Gu, C.; Ju, Y. Visible Light-Driven Photocatalytic Degradation of Rhodamine B over NaBiO3: Pathways and Mechanism. *J. Phys. Chem. A* **2009**, *113* (37), 10024−10032.

(40) Gavilán-Arriazu, E. M.; Mercer, M. P.; Barraco, D. E.; Hoster, H. E.; Leiva, E. P. M. Voltammetric Behaviour of LMO at the Nanoscale: A Map of Reversibility and Diffusional Limitations. *ChemPhysChem* **2022**, *23* (2), DOI: 10.1002/cphc.202100700.

(41) Nath, B. C.; Gogoi, B.; Boruah, M.; Sharma, S.; Khannam, M.; Ahmed, G. A.; Dolui, S. K. High Performance Polyvinyl Alcohol/Multi Walled Carbon Nanotube/Polyaniline Hydrogel (PVA/MWCNT/PAni) Based Dye Sensitized Solar Cells. *Electrochim. Acta* **2014**, *146*, 106−111.

(42) Kaliyaraj Selva Kumar, A.; Compton, R. G. Understanding Carbon Nanotube Voltammetry: Distinguishing Adsorptive and Thin Layer Effects via "Single-Entity" Electrochemistry. *J. Phys. Chem. Lett.* **2022**, *13* (24), 5557−5562.

(43) Elgrishi, N.; Rountree, K. J.; McCarthy, B. D.; Rountree, E. S.; Eisenhart, T. T.; Dempsey, J. L. A Practical Beginner's Guide to Cyclic Voltammetry. *J. Chem. Educ.* **2018**, *95* (2), 197−206.

(44) Sun, L.; Lu, J.; Chen, X.; Zhao, H.; Liu, L.; Yao, J. Cellulose Nanofiber Powered Interface Engineering Strategy to Manufacture Mechanically Stable, Moldable, Recyclable, and Biodegradable Cellulose Foam. *Chemical Engineering Journal* **2024**, *498*, 155155.

(45) Liu, Q.; Li, Y.; Yang, X.; Xing, S.; Qiao, C.; Wang, S.; Xu, C.; Li, T. O-Carboxymethyl Chitosan-Based PH-Responsive Amphiphilic Chitosan Derivatives: Characterization, Aggregation Behavior, and Application. *Carbohydr. Polym.* **2020**, *237*, 116112.

(46) Gong, X.; Zhao, C.; Wang, Y.; Luo, Y.; Zhang, C. Antifreezing, Ionically Conductive, Transparent, and Antidrying Carboxymethyl Chitosan Self-Healing Hydrogels as Multifunctional Sensors. *ACS Biomater Sci. Eng.* **2022**, *8* (8), 3633−3643.

(47) Song, P.; Xu, Z.; Guo, Q. Bioinspired Strategy to Reinforce PVA with Improved Toughness and Thermal Properties via Hydrogen-Bond Self-Assembly. *ACS Macro Lett.* **2013**, *2* (12), 1100−1104.

(48) Kwong, L. H.; Wilson, R.; Kumar, S.; Crider, Y. S.; Reyes Sanchez, Y.; Rempel, D.; Pillarisetti, A. Review of the Breathability and Filtration Efficiency of Common Household Materials for Face Masks. *ACS Nano* **2021**; 5904−5924, DOI: 10.1021/acsnano.0c10146.

(49) Vollmer, W.; Bertsche, U. Murein (Peptidoglycan) Structure, Architecture and Biosynthesis in Escherichia Coli. *Biochimica et Biophysica Acta - Biomembranes* **2008**, *1778*, 1714−1734.